

## Article

# Effect of Mn Element on the Structures and Properties of A<sub>2</sub>B<sub>7</sub>-Type La–Y–Ni-Based Hydrogen Storage Alloys

Anqiang Deng<sup>1,2,3</sup>, Yongchun Luo<sup>1,2,\*</sup>, Jianfei Zhou<sup>1</sup>, Yunding Xie<sup>1</sup>, Yuan Yuan<sup>1</sup>, Xiaoyan Kang<sup>1</sup>, Bingjin Shen<sup>1</sup> and Haimin Zhang<sup>1</sup>

<sup>1</sup> School of Materials Science and Engineering, Lanzhou University of Technology, Lanzhou 730050, China; deng\_aq@nxu.edu.cn (A.D.); maktub1998@163.com (J.Z.); 18438593522@163.com (Y.X.); 19831026757@163.com (Y.Y.); 18832029840@163.com (X.K.); aj18298343832@163.com (B.S.); zhbm@lut.edu.cn (H.Z.)

<sup>2</sup> State Key Laboratory of Advanced Processing and Recycling of Nonferrous Metals, Lanzhou University of Technology, Lanzhou 730050, China

<sup>3</sup> School of Mechanical Engineering, Ningxia University, Yinchuan 750021, China

\* Correspondence: luoyc@lut.edu.cn; Tel.: +86-931-2976688; Fax: +86-931-2976578

**Abstract:** The structures, hydrogen storage behaviors and electrochemical properties of Y<sub>0.75</sub>La<sub>0.25</sub>Ni<sub>3.5-x</sub>Mn<sub>x</sub> ( $x = 0-0.3$ ) alloys were analyzed by X-ray diffraction, Neutron powder diffraction, pressure–composition isotherms and electrochemical tests. All alloys have a multiphase structure. With the increase in Mn content, the Gd<sub>2</sub>Co<sub>7</sub>-type phase of the alloys gradually transforms into the Ce<sub>2</sub>Ni<sub>7</sub>-type phase; the Mn atom mainly occupies the Ni sites in the [AB<sub>5</sub>] subunit and the interface between the [AB<sub>5</sub>] and [A<sub>2</sub>B<sub>4</sub>] subunits; the  $V_{[A_2B_4]}/V_{[AB_5]}$  continuously decreases from 1.045 ( $x = 0$ ) to 1.019 ( $x = 0.3$ ), which reduces the volume mismatch between [A<sub>2</sub>B<sub>4</sub>] and [AB<sub>5</sub>] subunits. The maximum hydrogen absorption of the series alloys increases first and then decreases, and the addition of Mn effectively promotes the hydrogen absorption/desorption performance of the alloys. The maximum discharge capacity of the alloy electrodes is closely related to their hydrogen storage capacity at 0.1 MPa and hydrogen absorption/desorption plateau pressure. The cyclic stability of all the Mn-containing alloy electrodes is improved clearly compared to that of Mn-free alloy electrodes, because the volume mismatch between the [AB<sub>5</sub>] and [A<sub>2</sub>B<sub>4</sub>] subunits of the alloys becomes smaller after the addition of Mn, which can improve the structural stability and reduce the corrosion of alloys during hydrogen absorption/desorption cycles. When the Mn content is between 0.1 and 0.15, the Ce<sub>2</sub>Ni<sub>7</sub>-type phase of the alloys has high abundance and the alloy electrodes exhibit excellent overall performance.

**Keywords:** structures and properties; A<sub>2</sub>B<sub>7</sub>-type; La–Y–Ni-based; hydrogen storage alloys



**Citation:** Deng, A.; Luo, Y.; Zhou, J.; Xie, Y.; Yuan, Y.; Kang, X.; Shen, B.; Zhang, H. Effect of Mn Element on the Structures and Properties of A<sub>2</sub>B<sub>7</sub>-Type La–Y–Ni-Based Hydrogen Storage Alloys. *Metals* **2022**, *12*, 1122. <https://doi.org/10.3390/met12071122>

Academic Editors: Jacques Huot, Fusheng Yang and Giovanni Capurso

Received: 1 June 2022

Accepted: 27 June 2022

Published: 30 June 2022

**Publisher's Note:** MDPI stays neutral with regard to jurisdictional claims in published maps and institutional affiliations.



**Copyright:** © 2022 by the authors. Licensee MDPI, Basel, Switzerland. This article is an open access article distributed under the terms and conditions of the Creative Commons Attribution (CC BY) license (<https://creativecommons.org/licenses/by/4.0/>).

## 1. Introduction

The proposal of the goal of “carbon peak and carbon neutrality” will promote the rapid development of green energy vehicles. The large-scale application of new energy vehicles, such as pure electric vehicles (EVs), hybrid electric vehicles (HEVs) and fuel cell vehicles (FCVs), has put forward new requirements for power batteries [1–4]. Among the large number of rechargeable batteries, the nickel-metal hydride (Ni-MH) battery plays an important role in the battery-powered electric vehicle market, especially in hybrid electric vehicles, because of its excellent high-rate and low-temperature discharge capabilities, resistance to overcharge/discharge ability and significant safety [5–7].

Hydrogen storage alloys are used as Ni-MH anode materials, and their structure and properties affect the performance of batteries. Compared with traditional AB<sub>5</sub>-type (A is a rare earth; B is a transition metal) hydrogen storage alloys, La–Mg–Ni-based superlattice hydrogen storage alloys have the advantages of easy activation, high discharge capacity and high kinetic performance, so they have received considerable attention as negative

electrode materials for advanced nickel-metal hydride (Ni-MH) batteries [5,8–13]. However, the key element, Mg, in La–Mg–Ni system alloys is volatile at high temperatures. Therefore, it is not only difficult to control the composition but also has potential safety hazards during the preparation of La–Mg–Ni alloys [14,15].

The superlattice structure alloys are formed by stacking the  $[A_2B_4]$  subunit (Laves-type structure) and  $[AB_5]$  (CaCu<sub>5</sub>-type structure) subunit along the *c*-axis [16]. La<sub>2</sub>Ni<sub>7</sub> alloy is prone to hydrogen-induced amorphization, hydrogen-induced phase transformation and disproportionation during the hydrogen absorption/desorption process [17–19]. This is mainly due to the large volume mismatch between the  $[La_2Ni_4]$  and  $[LaNi_5]$  subunits, and hydrogen only enters into the  $[La_2Ni_4]$  subunit and not into the  $[LaNi_5]$  subunit, which causes the “anisotropic expansion” of the alloy during hydrogenation. After adding Mg to La<sub>2</sub>Ni<sub>7</sub> alloy, since the atomic radius of Mg ( $R_{Mg} = 1.72 \text{ \AA}$ ) is smaller than that of La ( $R_{La} = 2.74 \text{ \AA}$ ), and Mg only occupies the La sites in the  $[A_2B_4]$  subunit, with the addition of Mg, the volume mismatch between the  $[A_2B_4]$  and  $[AB_5]$  subunits reduces, which effectively improves the hydrogen absorption/desorption properties of the alloys [20,21]. Unlike La<sub>2</sub>Ni<sub>7</sub>, Latroche et al. [22] found that the hydrogen storage capacity of Y<sub>2</sub>Ni<sub>7</sub> alloy did not decay after several hydrogen absorption/desorption cycles at 0.1 and 0.7 MPa, and the alloy structure remained unchanged, but there were three hydrogen absorption/desorption plateaus at 10 MPa and the plateau pressures were higher (0.055 MPa, 0.5 MPa, 2.9 MPa); therefore, Y<sub>2</sub>Ni<sub>7</sub> alloy was not properly used as an alloy electrode material. Paul-Boncour et al. [23] studied the La<sub>2–x</sub>Y<sub>x</sub>Ni<sub>7</sub> ( $x = 0–2$ ) alloy and found that Y preferentially occupies La sites in the  $[A_2B_4]$  subunit and the atomic radius of Y ( $R_Y = 2.27 \text{ \AA}$ ) is smaller than that of La ( $R_{La} = 2.74 \text{ \AA}$ ); the addition of Y in La–Y–Ni alloys helps to adjust the volume mismatch between the  $[A_2B_4]$  and  $[AB_5]$  subunits. Therefore, the effect of Y in La–Y–Ni alloys is similar to the Mg in La–Mg–Ni alloys. In addition, Yuan et al. [14] studied the La<sub>3–x</sub>Y<sub>x</sub>Ni<sub>9.7</sub>Mn<sub>0.5</sub>Al<sub>0.3</sub> ( $x = 1, 1.5, 1.75, 2, 2.25, 2.5$ ) alloys and found that the alloy electrodes had better overall electrochemical performance when  $x = 1.75–2.25$ .

In traditional AB<sub>5</sub>-type hydrogen storage alloys, Mn is an essential and key element, which occupies the 3*g* and 2*c* positions in the CaCu<sub>5</sub> structure, and is more effective in adjusting the hydrogen absorption/desorption plateau pressure than Al for AB<sub>5</sub>-type alloys [24]. In La–Mg–Ni alloys, the substitution of Mn for Ni can not only decrease the plateau equilibrium pressure and increase the discharge capacity [25], but also increase the catalytic activity of the alloy electrode [26,27]. At the same time, the A<sub>2</sub>B<sub>7</sub>-type superlattice hydrogen storage alloys have attracted much attention as new-generation nickel-metal hydride battery anode materials [28–30].

In this study, we selected Y<sub>0.75</sub>La<sub>0.25</sub>Ni<sub>3.5</sub> alloy as the original alloy, and the effect of the Mn element on the structures and properties of A<sub>2</sub>B<sub>7</sub>-type La–Y–Ni-based hydrogen storage alloys was investigated systematically. This study will offer a guide for further developing the La–Y–Ni system hydrogen storage alloys.

## 2. Materials and Methods

### 2.1. Sample Preparation

Y<sub>0.75</sub>La<sub>0.25</sub>Ni<sub>3.5–x</sub>Mn<sub>x</sub> ( $x = 0, 0.05, 0.1, 0.15, 0.2, 0.3$ ) hydrogen storage alloys were prepared by arc melting under a 0.05 MPa argon (Ar) atmosphere, and as-cast alloys were melted three times to obtain a homogeneous ingot. Subsequent annealing was performed for 24 h at 1173 K in a 0.2 MPa argon (Ar) atmosphere. The purity of all component elements was above 99 wt.%. In order to compensate for the evaporative loss, an appropriate excess of some component metals (5 wt.% for La, Y and 8% for Mn) was added, respectively.

### 2.2. Structure Characterization

The annealed alloys were crushed mechanically by hand in an agate mortar, and sieved through a 200–300 size mesh for X-ray diffraction (XRD) measurements, 50 size mesh for neutron powder diffraction (NPD) measurements and 200–300 size mesh for alloy electrodes. XRD measurements were performed on a Bruker D8 Advance diffrac-

tometer (Bruker Corporation, Karlsruhe, Germany) with Cu radiation and a power of  $40 \text{ kV} \times 40 \text{ mA}$ . The patterns were recorded over the range from  $8^\circ$  to  $120^\circ$  in  $2\theta$  by steps of  $0.02^\circ$ . NPD was analyzed with  $\lambda = 1.8846 \text{ \AA}$  by a step size of  $0.02^\circ$  in the range  $12\text{--}150^\circ$  at room temperature. Then, the XRD and NPD collected data were analyzed by the Rietveld method [31] using the Fullprof program (March 2021, Institut Laue-Langevin, Grenoble, France) [32].

### 2.3. Hydrogen Absorption and Desorption Measurements

Pressure–composition isotherm (P–C–T) tests were performed using a Sieverts-type apparatus (Beijing Nonferrous Metal Research Institute, Beijing, China) at 298 K. Prior to formal measurements, powder samples were evacuated at 373 K and  $1 \times 10^{-4} \text{ Pa}$  for at least 2 h in a resistance furnace to remove the impurities. In order to ensure that the sample was completely activated, the sample was hydrided under 8 MPa for 2 h and dehydrided at 0.001 MPa for approximately 2 h, several times.

### 2.4. Electrochemical Measurements

Alloy electrodes were prepared by cold pressing the mixture of alloy powder and carbonyl nickel powder with the weight ratio of 1:3 under 20 MPa pressure to form a pellet of 10 mm in diameter. Electrochemical measurements were performed at 298 K in a standard open tri-electrode electrolysis cell, in which the alloy electrode was used as the working electrode, the  $\text{Ni}(\text{OH})_2/\text{NiOOH}$  electrode as the counter electrode, the Hg/HgO electrode as the reference electrode and KOH solution (6 M) as the electrolyte. Each electrode was discharged to cut-off potential  $-0.6 \text{ V}$  Vs. Hg/HgO reference electrode.

Alloy electrodes were charged/discharged at  $100 \text{ mA g}^{-1}$  when activated and examined for cyclic stability. The cyclic stability was identified by the capacity retention after the 100th cycle with the following equation [33]:

$$S_{100} = \frac{C_{100}}{C_{\max}} \times 100\% \quad (1)$$

where  $C_{100}$  and  $C_{\max}$  were the discharge capacity at the 100th cycle and the maximum discharge capacity, respectively.

To analyze the corrosion behaviors of the alloy electrodes, a corrosion polarization curve (Tafel polarization curve) was acquired on a CHI660A electrochemical work station (Shanghai Chenhua Instrument Co., Ltd., Shanghai, China) after the alloy electrodes were activated. The Tafel polarization curves were measured by scanning the electrode potential at a rate of  $1 \text{ mV s}^{-1}$  from  $-250$  to  $250 \text{ mV}$  (vs. open circuit potential) at 50% depth of discharge (DOD).

## 3. Results and Discussion

### 3.1. Crystal Structure

Figures 1 and 2 show the XRD and the Rietveld refinement pattern of  $\text{Y}_{0.75}\text{La}_{0.25}\text{Ni}_{3.5-x}\text{Mn}_x$  ( $x = 0, 0.05, 0.1, 0.15, 0.2, 0.3$ ) annealed alloys; crystallographic parameters obtained by the Rietveld whole pattern fitting method are tabulated in Table 1. It can be seen that  $\text{Y}_{0.75}\text{La}_{0.25}\text{Ni}_{3.5}$  alloy consists of complex phases, which can be identified as  $\text{PuNi}_3$ -type (SG:  $R\text{-}3m$ ),  $\text{Ce}_2\text{Ni}_7$ -type (Space group:  $P6_3/mmc$ ),  $\text{Gd}_2\text{Co}_7$ -type (Space group:  $R\text{-}3m$ ),  $\text{Ce}_5\text{Co}_{19}$ -type (Space group:  $R\text{-}3m$ ) and  $\text{CaCu}_5$ -type phase (Space group:  $P6/mmm$ ). When  $x = 0.05$ , a small amount of Mn substitution for Ni does not change the phase structure of the alloys, but the  $\text{Gd}_2\text{Co}_7$ -type phase decreases while the  $\text{Ce}_2\text{Ni}_7$ - and  $\text{CaCu}_5$ -type phases increase. With further increasing Mn content, the  $\text{Gd}_2\text{Co}_7$ -type phase transforms to the  $\text{Ce}_2\text{Ni}_7$ -type phase gradually, the  $\text{Gd}_2\text{Co}_7$ -type phase continues to decrease and the  $\text{Ce}_2\text{Ni}_7$ -type phase becomes the main phase of the alloys, which is mainly ascribed to the atomic radius of Mn ( $R_{\text{Mn}} = 1.79 \text{ \AA}$ ) being larger than that of Ni ( $R_{\text{Ni}} = 1.62 \text{ \AA}$ ).  $\text{R}_2\text{Ni}_7$  compounds are polymorphic; they crystallize either in the  $P6_3/mmc$  (2H) or  $R\text{-}3m$  (3R) space group. Buschow et al. [34] found that the crystal structure of rare-earth nickel-based

$R_2Ni_7$ -type alloys depended on their R atomic radius: when the R atomic radius is large, the  $R_2Ni_7$  alloy can easily form a  $2H-Ce_2Ni_7$  structure, while, when the R atomic radius is small, the  $R_2Ni_7$  alloy is prone to form a  $3R-Gd_2Co_7$  structure. When Mn = 0.1 and 0.15, the abundance of  $Ce_2Ni_7$ -type phase in the alloy reaches 84% and 93%, respectively. As Mn further increases, the  $PuNi_3$ -type phase increases and  $Ce_2Ni_7$ -type phase abundance decreases again. Therefore, if the content of Mn is too low, the  $Gd_2Co_7$ -type phase exists in the alloy; on the contrary, if the Mn content is too high, the  $PuNi_3$ -type phase increases. When the content of Mn is between 0.1 and 0.15, the alloys have an approximately single-phase structure, where the abundance of the  $Ce_2Ni_7$ -type phase reaches more than 80%. The variation trend of phase abundance as a function of the Mn content of alloys is presented in Figure 3.

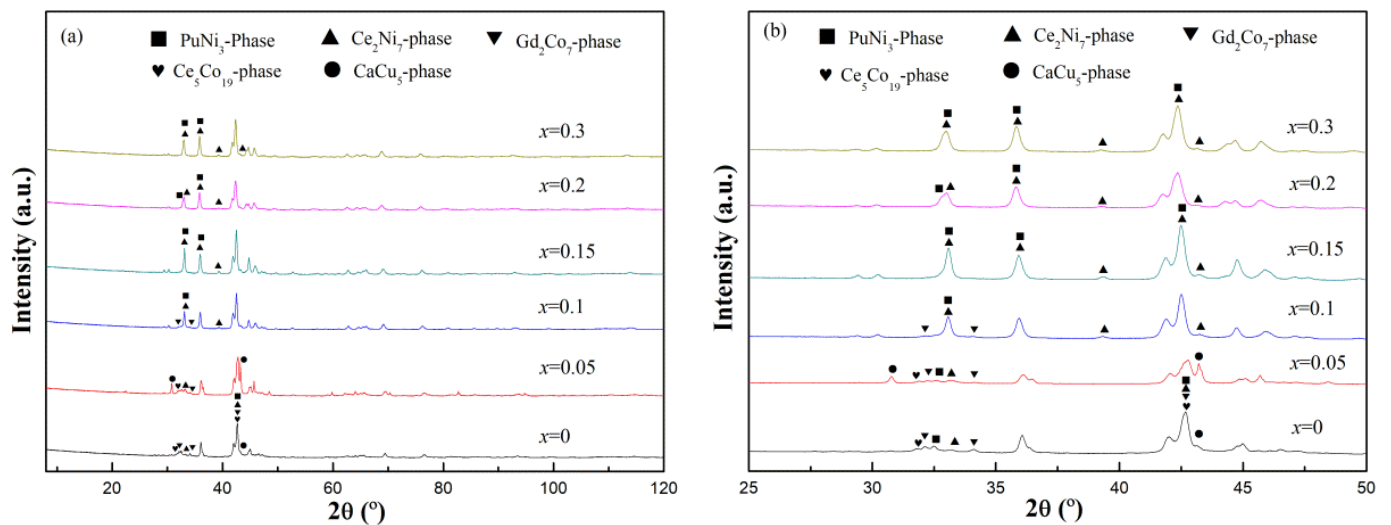


**Figure 1.** XRD pattern of  $Y_{0.75}La_{0.25}Ni_{3.5-x}Mn_x$  ( $x = 0-0.3$ ) annealed alloys: (a) whole pattern; (b) local pattern.

**Table 1.** Crystallographic data of  $Y_{0.75}La_{0.25}Ni_{3.5-x}Mn_x$  ( $x = 0-0.3$ ) annealed alloys.

Sample (x)	Phase	Space Group	Phase Abundance (%)	Lattice Constant			
				a (Å)	c (Å)	V (Å <sup>3</sup> )	cla
x = 0	PuNi <sub>3</sub>	R-3m	24(1)	4.934(3)	24.755(2)	521.86(4)	5.017
	Ce <sub>2</sub> Ni <sub>7</sub>	P6 <sub>3</sub> /mmc	19(1)	4.978(1)	24.166(1)	518.97(10)	4.853
	Gd <sub>2</sub> Co <sub>7</sub>	R-3m	37(1)	4.975(1)	36.446(2)	781.23(6)	7.326
	Ce <sub>5</sub> Co <sub>19</sub>	R-3m	17(1)	4.977(1)	48.327(4)	1036.8(2)	9.710
	CaCu <sub>5</sub>	P6/mmm	3(1)	4.922(1)	3.9756(1)	83.407(1)	0.808
x = 0.05	PuNi <sub>3</sub>	R-3m	11(1)	4.956(1)	24.736(1)	526.07(18)	4.992
	Ce <sub>2</sub> Ni <sub>7</sub>	P6 <sub>3</sub> /mmc	28(1)	4.986(1)	24.202(1)	521.08(6)	4.854
	Gd <sub>2</sub> Co <sub>7</sub>	R-3m	14(1)	4.986(1)	36.425(1)	784.09(6)	7.306
	Ce <sub>5</sub> Co <sub>19</sub>	R-3m	18(1)	4.968(2)	48.230(3)	1031.0(1)	9.708
	CaCu <sub>5</sub>	P6/mmm	29(1)	4.927(2)	3.9722(1)	83.523(1)	0.806
x = 0.1	PuNi <sub>3</sub>	R-3m	6(1)	4.974(1)	24.682(2)	528.83(7)	4.962
	Ce <sub>2</sub> Ni <sub>7</sub>	P6 <sub>3</sub> /mmc	84(1)	4.993(1)	24.241(5)	523.42(2)	4.855
	Gd <sub>2</sub> Co <sub>7</sub>	R-3m	10(1)	4.993(1)	36.418(29)	786.22(10)	7.294
x = 0.15	PuNi <sub>3</sub>	R-3m	7(1)	5.008(1)	24.581(14)	533.88(4)	4.908
	Ce <sub>2</sub> Ni <sub>7</sub>	P6 <sub>3</sub> /mmc	93(1)	4.997(1)	24.287(3)	525.15(1)	4.861
x = 0.2	PuNi <sub>3</sub>	R-3m	30(1)	5.018(1)	24.532(1)	534.93(2)	4.889
	Ce <sub>2</sub> Ni <sub>7</sub>	P6 <sub>3</sub> /mmc	70(1)	5.003(1)	24.328(1)	527.33(2)	4.863
x = 0.3	PuNi <sub>3</sub>	R-3m	38(1)	5.020(1)	24.500(6)	534.71(2)	4.880
	Ce <sub>2</sub> Ni <sub>7</sub>	P6 <sub>3</sub> /mmc	62(1)	5.010(1)	24.369(1)	529.65(1)	4.864

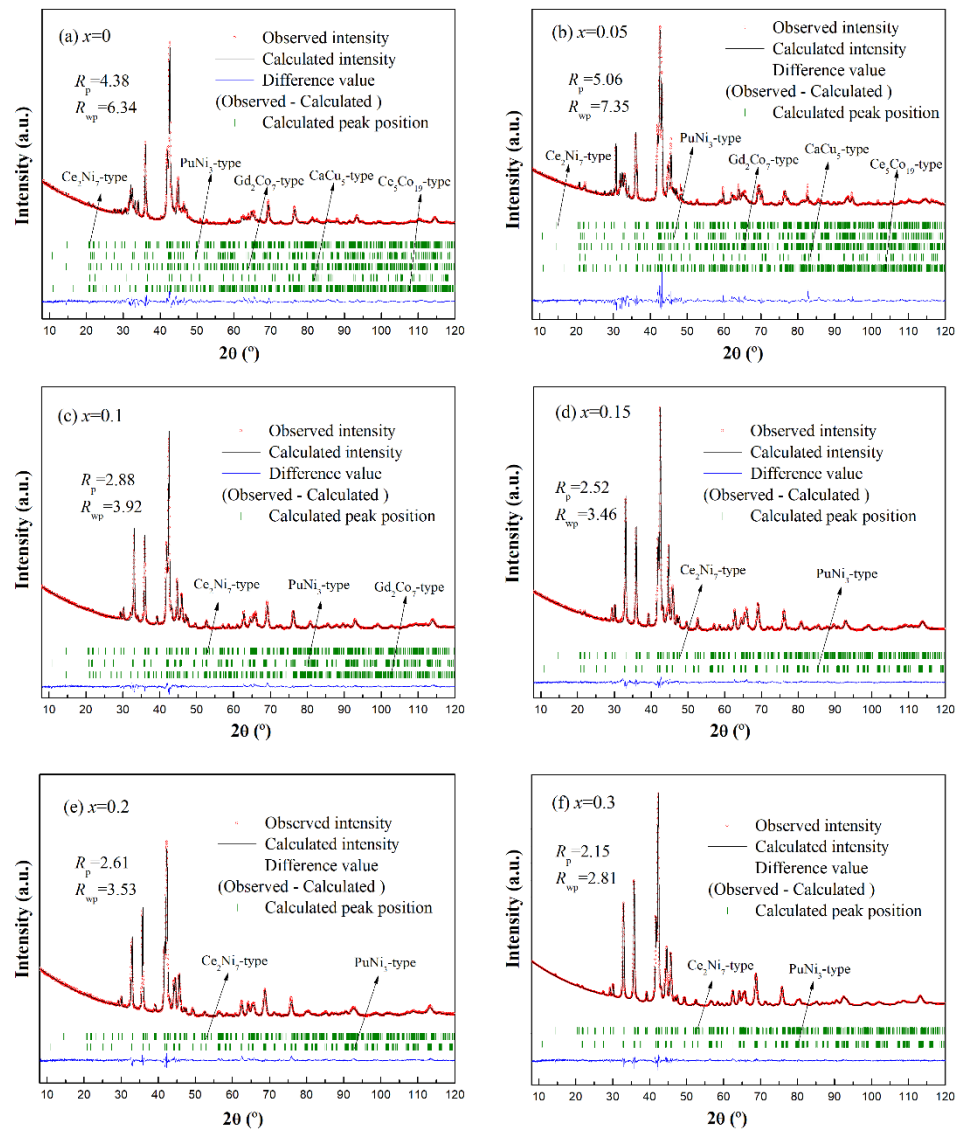


Figure 2. Rietveld refinement pattern of the XRD data for  $Y_{0.75}La_{0.25}Ni_{3.5-x}Mn_x$  ( $x = 0, 0.05, 0.1, 0.15, 0.2, 0.3$ ) alloys: (a)  $x = 0$ ; (b)  $x = 0.05$ ; (c)  $x = 0.1$ ; (d)  $x = 0.15$ ; (e)  $x = 0.2$ ; (f)  $x = 0.3$ .

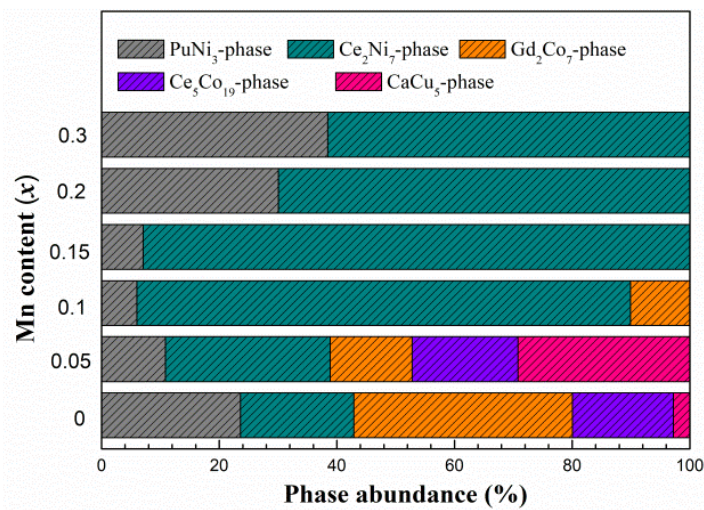
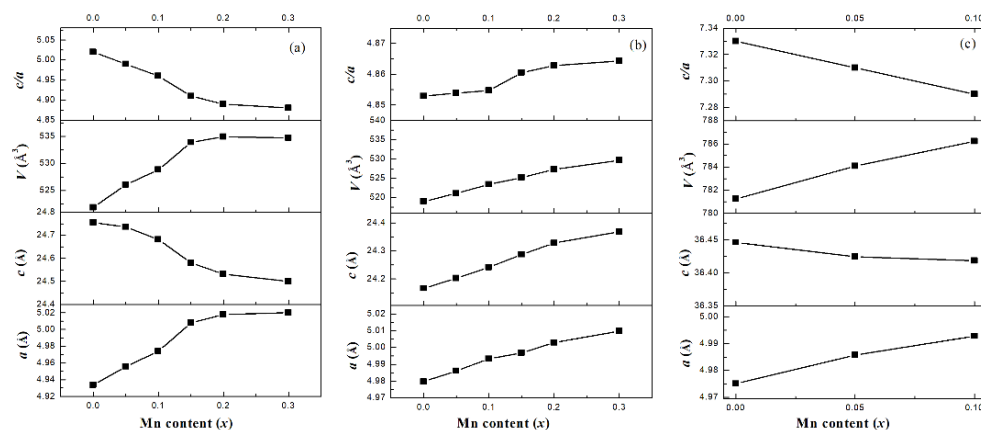


Figure 3. Phase abundance as a function of Mn content of  $Y_{0.75}La_{0.25}Ni_{3.5-x}Mn_x$  ( $x = 0-0.3$ ) annealed alloys.

Figure 4 shows the lattice constant variation of each phase as a function of the Mn content of the  $Y_{0.75}La_{0.25}Ni_{3.5-x}Mn_x$  ( $x = 0, 0.05, 0.1, 0.15, 0.2, 0.3$ ) annealed alloys. The atomic radius of Mn ( $R_{Mn} = 1.79 \text{ \AA}$ ) is larger than that of Ni ( $R_{Ni} = 1.62 \text{ \AA}$ ), so the unit cell volume of each phase becomes larger after Mn is added. The  $PuNi_3$ -type phase increases from  $521.86 \text{ \AA}^3$  ( $x = 0$ ) to  $534.71 \text{ \AA}^3$  ( $x = 0.3$ ),  $Ce_2Ni_7$ -type phase increases from  $518.97 \text{ \AA}^3$  ( $x = 0$ ) to  $529.65 \text{ \AA}^3$  at ( $x = 0.3$ ), and  $Gd_2Co_7$ -type phase increases from  $781.23 \text{ \AA}^3$  ( $x = 0$ ) to  $786.22 \text{ \AA}^3$  at ( $x = 0.1$ ), respectively. It is worth nothing that the lattice constant  $a$  of the three phases increases, whereas the lattice constant  $c$  changes differently; the  $c$  value increases in the  $Ce_2Ni_7$ -type type phase, and it remains basically unchanged in the  $Gd_2Co_7$ -type phase, but decreases in the  $PuNi_3$ -type phase. This may be related to the selective occupation in the space lattice of Mn atoms in each phase.



**Figure 4.** Lattice constant of  $PuNi_3$ -type (a),  $Ce_2Ni_7$ -type (b),  $Gd_2Co_7$ -type (c) phase as a function of Mn content for  $Y_{0.75}La_{0.25}Ni_{3.5-x}Mn_x$  ( $x = 0-0.3$ ) annealed alloys.

Because the atomic numbers of Ni (25) and Mn (28) are relatively close, it is difficult to accurately distinguish the atomic occupancy of the two elements by XRD. The neutron scattering length of Mn is negative ( $-0.373 \times 10^{-12} \text{ cm}$ ) while that of Ni is positive ( $+1.03 \times 10^{-12} \text{ cm}$ ) [35]; there is a large difference between them. Therefore, neutron diffraction can easily characterize the occupancy of Ni and Mn in B-site elements of La-Y-Ni-Mn hydrogen storage alloys. Figure 5 shows the Rietveld refinement of the NPD pattern for  $Y_{0.75}La_{0.25}Ni_{3.2}Mn_{0.3}$  alloys, Table 2 lists the crystal structure data of the  $PuNi_3$ -type (Table 2(a)) and  $Ce_2Ni_7$ -type phases (Table 2(b)), and Figure 6 presents the schematic diagram of the atomic stacking along the  $c$ -axis of the two phases. The results show that Mn occupies the  $6c$  site in the  $[AB_5]$  subunit and a small amount of Mn occupies the  $18h$  site of the interface between the  $[A_2B_4]$  and  $[AB_5]$  subunits of the  $PuNi_3$ -type phase, while Mn only occupies the  $4e$  and  $6h$  sites in the  $[AB_5]$  subunit of the  $Ce_2Ni_7$ -type phase.

The superlattice structure is described as stacking structures made of  $[A_2B_4]$  and  $[AB_5]$  subunits piled along the  $c$ -axis. Their general formula, summarized by Khan [36], can be defined as  $y = (5n + 4)/(n + 2)$  (where  $n$  is the number of  $[AB_5]$  subunits). For  $A_2B_7$  alloy,  $n$  is equal to 2 and, consequently, the basic period can be defined as  $[A_2B_4] + 2[AB_5]$ . These phases are polymorphs as they crystallize either in hexagonal ( $2H$ ,  $Ce_2Ni_7$ -type) or rhombohedral ( $3R$ ,  $Gd_2Co_7$ -type) symmetry. As long as the volume of the  $[A_2B_4]$  subunit is larger than that of the  $[AB_5]$  subunit, the  $[A_2B_4]$  subunit remains more active with respect to hydrogenation [37]. In other words, for superlattice structure hydrogen storage alloys, the larger the volume mismatch of  $V_{[A_2B_4]}/V_{[AB_5]}$  is, the more obvious the "anisotropic" expansion of the lattice will be during hydrogen absorption/desorption. The structural evolution of the hydrogen absorption/desorption of  $La_2Ni_7$  [17] alloy is the most typical example. Figure 7 shows the variation of the  $[A_2B_4]$  and  $[AB_5]$  subunits as a function of the Mn content of the  $Ce_2Ni_7$ -type phase. It is clear that the volume of the  $[AB_5]$  subunit increases almost linearly with increasing Mn content, from  $85.22 \text{ \AA}^3$  ( $x = 0$ ) to  $87.72 \text{ \AA}^3$  ( $x = 0.3$ ), while the volume of the  $[A_2B_4]$  subunit is almost unchanged;

the results also indicate that Mn mainly occupies Ni sites in the [AB<sub>5</sub>] subunit, and this is in good agreement with the atomic occupancy (Table 2) obtained from NPD data. In addition,  $V_{[A_2B_4]}/V_{[AB_5]}$  decreases gradually, from 1.045 ( $x = 0$ ) to 1.019 ( $x = 0.3$ ). This is mainly due to the atomic radius of Mn being larger than that of Ni, and its selective occupation in the superlattice structure. The smaller the volume mismatch in  $V_{[A_2B_4]}/V_{[AB_5]}$  is, the better the structural stability of the alloys will be during hydrogen absorption/desorption [38,39].

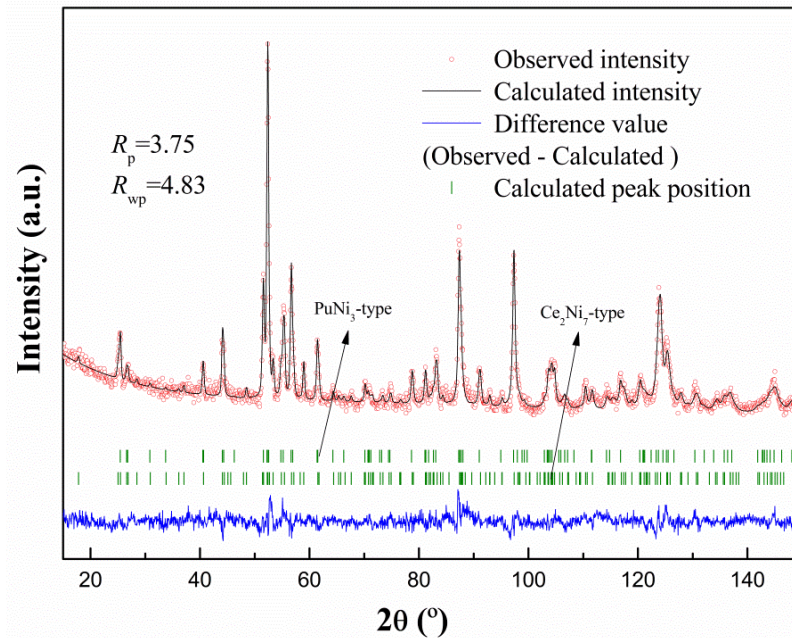


**Figure 5.** Rietveld refinement of the NPD pattern for  $Y_{0.75}La_{0.25}Ni_{3.2}Mn_{0.3}$  alloys.

**Table 2.** a. Crystal structure data of PuNi<sub>3</sub>-type phase for  $Y_{0.75}La_{0.25}Ni_{3.2}Mn_{0.3}$  annealed alloys. b. Crystal structure data of Ce<sub>2</sub>Ni<sub>7</sub>-type phase for  $Y_{0.75}La_{0.25}Ni_{3.2}Mn_{0.3}$  annealed alloys.

(a)						
Site	Atom	$x$	$y$	$z$	$B_{iso}(\text{Å}^2)$	Occupancy
3a	La	0	0	0	1.9(2)	0.28(4)
	Y	0	0	0	1.9(2)	0.72(4)
6c	La	0	0	0.1418(7)	0.4(1)	0.11(2)
	Y	0	0	0.1418(7)	0.4(1)	0.89(2)
3b	Ni	0	0	0.5	0.6(1)	1
6c	Ni	0	0	0.3317(9)	2.5(2)	0.75(3)
	Mn	0	0	0.3317(9)	2.5(2)	0.25(3)
18h	Ni	0.4999(12)	−0.4999(12)	0.0830(4)	0.3(1)	0.96(1)
	Mn	0.4999(12)	−0.4999(12)	0.0830(4)	0.3(1)	0.04(1)
(b)						
Site	Atom	$x$	$y$	$z$	$B_{iso}(\text{Å}^2)$	Occupancy
4f1	Y	0	0	0.0282(6)	2.7(2)	1
4f2	La	0	0	0.1717(6)	1.7(2)	0.58(5)
	Y	0	0	0.1717(6)	1.7(2)	0.42(5)
2a	Ni	0	0	0	1.9(2)	1
4e	Ni	0	0	0.1671(8)	1.1(2)	0.77(6)
	Mn	0	0	0.1671(8)	1.1(2)	0.23(6)
4f	Ni	0.6667	0.3333	0.1666(6)	0.2(2)	1
6h	Ni	0.1621(6)	0.3241(12)	0.75	1.6(1)	0.68(5)
	Mn	0.1621(6)	0.3241(12)	0.75	1.6(1)	0.32(5)
12k	Ni	0.1689(7)	0.3377(14)	0.9156(3)	1.2(1)	1

$B_{iso}$ : Temperature factor; Occupancy: Atomic occupation.

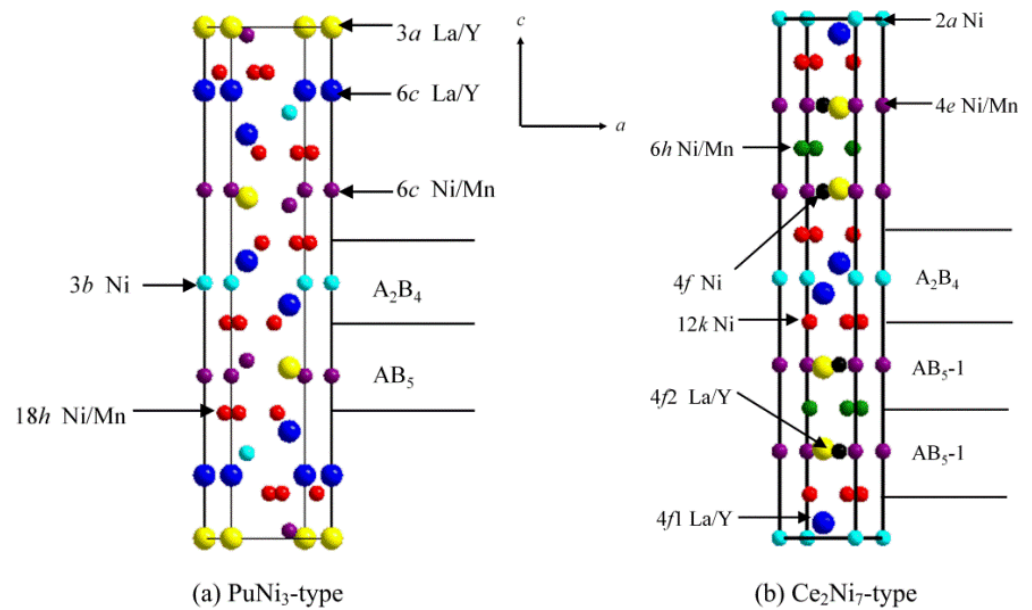


**Figure 6.** Representative structures of 3R-type  $\text{PuNi}_3$  (a) and 2H-type  $\text{Ce}_2\text{Ni}_7$  (b) stacked by  $[\text{A}_2\text{B}_4]$  and  $[\text{AB}_5]$  subunits along the  $c$ -axis in La-Y-Ni system hydrogen storage alloys with superlattice structure.

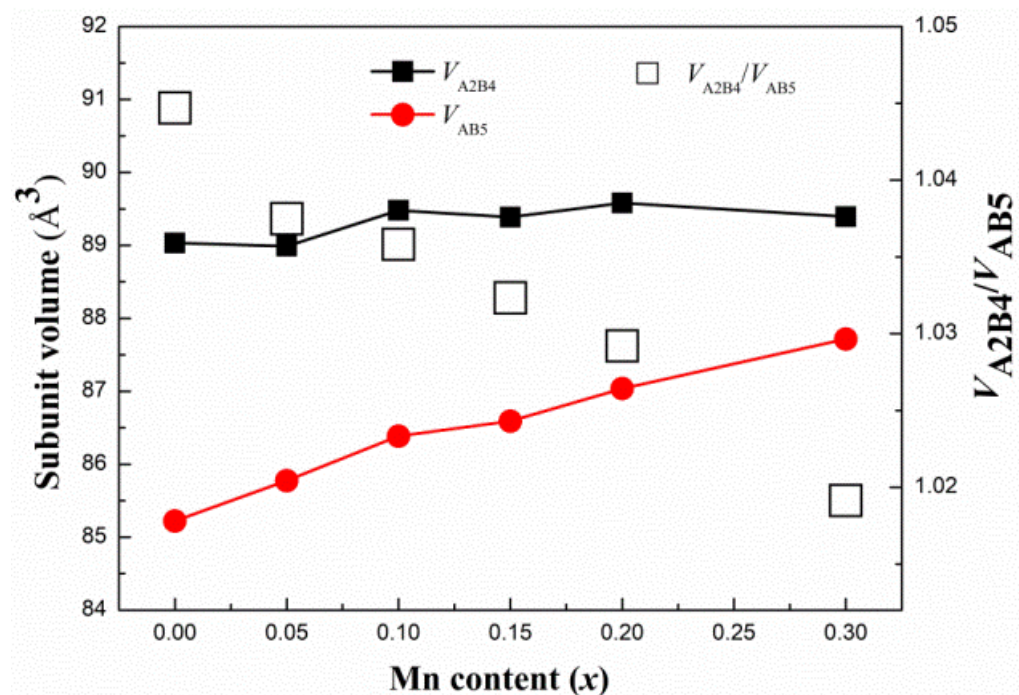


**Figure 7.** Subunit volume of  $\text{Ce}_2\text{Ni}_7$ -type phase for  $\text{Y}_{0.75}\text{La}_{0.25}\text{Ni}_{3.5-x}\text{Mn}_x$  ( $x = 0-0.3$ ) annealed alloys.

### 3.2. Hydrogen Storage Characteristics

Figure 8 shows the  $P$ - $C$  isotherm curves (gaseous hydrogen absorption/desorption) of  $\text{Y}_{0.75}\text{La}_{0.25}\text{Ni}_{3.5-x}\text{Mn}_x$  ( $x = 0, 0.05, 0.1, 0.15, 0.2, 0.3$ ) annealed alloy at 298 K. The basic data in the process of the hydrogen absorption/desorption of alloys are presented in Table 3. It can be found that all alloys are activated within three times; with the increase in Mn content, the hydrogen capacity and plateau pressure during hydrogen absorption/desorption change, which may be closely related to the phase structures and the corresponding unit cell volume of the alloys. This will be discussed in detail below.

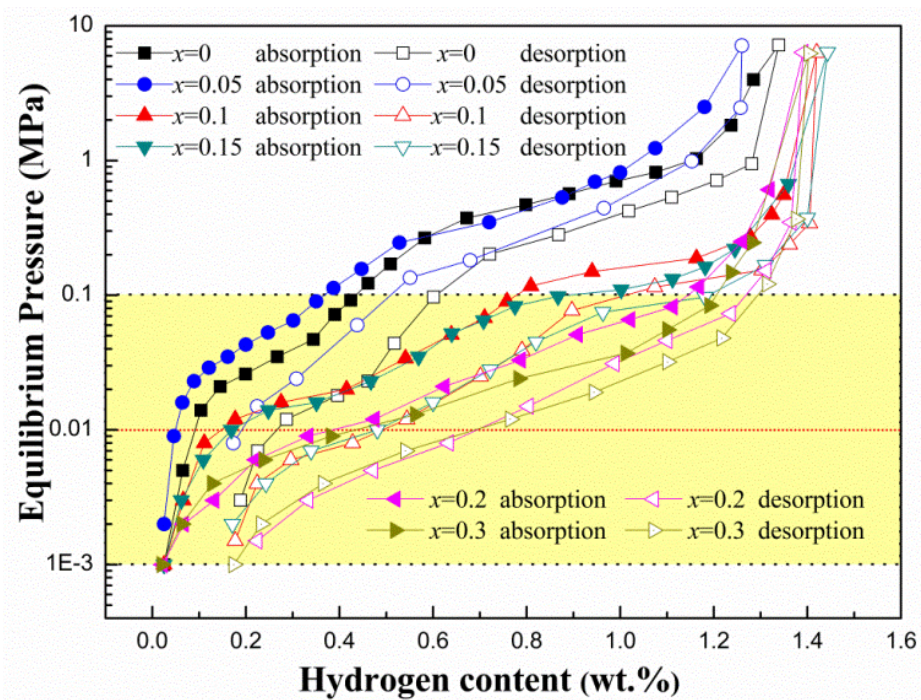


**Figure 8.** *P*-*C* isotherm curves (absorption and desorption) of  $Y_{0.75}La_{0.25}Ni_{3.5-x}Mn_x$  ( $x = 0-0.3$ ) annealed alloys at 298 K.

**Table 3.** Hydrogen absorption/desorption characteristics of  $Y_{0.75}La_{0.25}Ni_{3.5-x}Mn_x$  ( $x = 0-0.3$ ) annealed alloy.

Sample ( <i>x</i> )	Activation	Plateau Pressure		Hydrogen Capacity	Hydrogen Capacity
	Time	(MPa)		8 MPa	0.1 MPa
	$N_a$	Abs.	Des.	(wt.%)	(wt.%)
$x = 0.00$	3	0.05/0.67	0.01/0.39	1.34	0.44
$x = 0.05$	3	0.25/0.69	0.04/0.42	1.26	0.38
$x = 0.10$	3	0.03/0.02	0.01/0.13	1.42	0.79
$x = 0.15$	3	0.03/0.13	0.02/0.10	1.44	0.87
$x = 0.20$	3	0.03	0.02	1.40	1.16
$x = 0.30$	3	0.02	0.01	1.40	1.21

Abs: Absorption; Des: Desorption.

With the increase in Mn content, the unit cell volumes of all phases of La-Y-Ni-Mn alloys increase, which leads to a decrease in the plateau pressure during hydrogen absorption/desorption [10,40]. The hydrogen absorption plateau pressure decreased from 0.67 MPa ( $x = 0$ ) to 0.02 MPa ( $x = 0.3$ ), and the hydrogen desorption plateau pressure decreased from 0.39 MPa ( $x = 0$ ) to 0.01 MPa ( $x = 0.3$ ). This shows that Mn can effectively reduce the plateau pressure of the hydrogen absorption/desorption of La-Y-Ni system hydrogen storage alloys, which is consistent with the current research [15,41]. At the same time, with the rise of  $x$ , the hydrogen absorption/desorption plateau of the alloy becomes flatter and wider, indicating that the addition of Mn can effectively promote the hydrogen absorption and desorption properties of La-Y-Ni system alloys.

The maximum hydrogen absorption capacity of series alloys is 1.26 wt.%–1.44 wt.% under 8 MPa. When the Mn content increases, the maximum hydrogen absorption of the alloy increases first and then decreases, but the overall trend is increasing. It increases from 1.34 wt.% ( $x = 0$ ) to 1.44 wt.% ( $x = 0.15$ ) and then decreases to 1.40 wt.% ( $x = 0.3$ ); the increase in the maximum hydrogen absorption capacity ( $x = 0-0.15$ ) may be mainly due to the Mn effectively reducing the hydrogen absorption/desorption plateau pressure of the

alloys, while the decrease in the maximum hydrogen absorption capacity ( $x = 0.15\text{--}0.3$ ) is related to the fact that the hydrogen absorption/desorption plateau pressure of the alloy is so low that the hydrogen cannot be released. All alloys have relatively obvious hydrogen absorption/desorption plateaus, indicating that there is no serious hydrogen-induced amorphization during the hydrogen absorption/desorption process of the alloys. When the Mn content is low ( $x < 0.2$ ), the alloys have multiple hydrogen absorption/desorption plateaus, which is mainly ascribed to the alloys having a multiphase structure, and the unit cell volume of each phase is different. When the Mn content is high ( $x \geq 0.2$ ), the alloys have only two types of phases, PuNi<sub>3</sub>-type and Ce<sub>2</sub>Ni<sub>7</sub>-type, and the unit cell volumes of the two types of phases are almost the same, so the alloys have only one hydrogen absorption/desorption plateau.

### 3.3. Discharge and Cyclic Properties

Figure 9 shows the electrochemical  $P$ - $C$  isotherm curves (desorption) of  $\text{Y}_{0.75}\text{La}_{0.25}\text{Ni}_{3.5-x}\text{Mn}_x$  ( $x = 0\text{--}0.3$ ) annealed alloy electrodes at 298 K. It is found that the variation law of the electrochemical  $P$ - $C$  isotherm curves of the alloy electrodes is in good agreement with the  $P$ - $C$  isotherm curves of the alloy gaseous hydrogen desorption between  $10^{-3}$  and  $10^{-1}$  MPa. Except for  $x = 0.05$ , the hydrogen desorption plateau pressure of the alloy gradually decreases with the increase in Mn content. Figure 10 shows the 100 charge/discharge cycles curve of the alloy electrode at a charge/discharge current density of  $100 \text{ mA}\cdot\text{g}^{-1}$ . Figure 11 presents the relationship between the maximum discharge capacity and cyclic stability of the  $\text{Y}_{0.75}\text{La}_{0.25}\text{Ni}_{3.5-x}\text{Mn}_x$  ( $x = 0\text{--}0.3$ ) alloy electrode as a function of Mn content. Table 4 summarizes the electrochemical performance of the alloy electrodes. It can be seen that all of the alloy electrodes exhibit good activation properties; except for  $x = 0$  and  $0.05$ , the alloy electrodes were fully activated within five times, and the activation times of  $x = 0.05$  and  $0.1$  alloy electrodes exceeded three times, but all reached 90% of the maximum discharge capacity within three times. With the increase in  $x$ , the maximum discharge capacity of the alloy electrodes first increases and then decreases, from  $231.9 \text{ mAh}\cdot\text{g}^{-1}$  ( $x = 0$ ) to  $367.4 \text{ mAh}\cdot\text{g}^{-1}$  ( $x = 0.15$ ), and then decreases to  $334.4 \text{ mAh}\cdot\text{g}^{-1}$  ( $x = 0.3$ ).

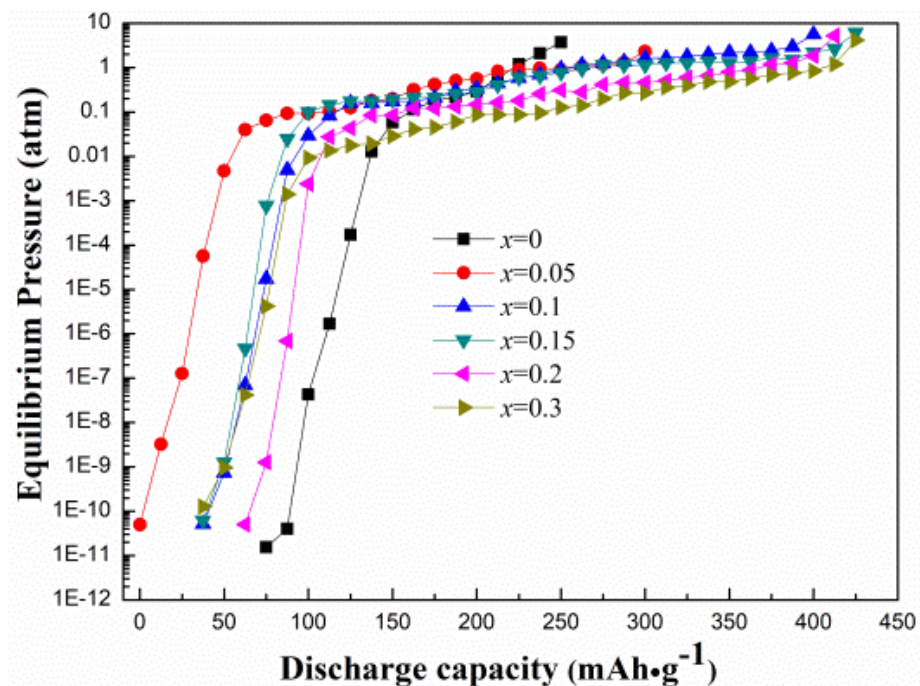


**Figure 9.** Electrochemical  $P$ - $C$  isotherm curves (desorption) of  $\text{Y}_{0.75}\text{La}_{0.25}\text{Ni}_{3.5-x}\text{Mn}_x$  ( $x = 0\text{--}0.3$ ) annealed alloys at 298 K.

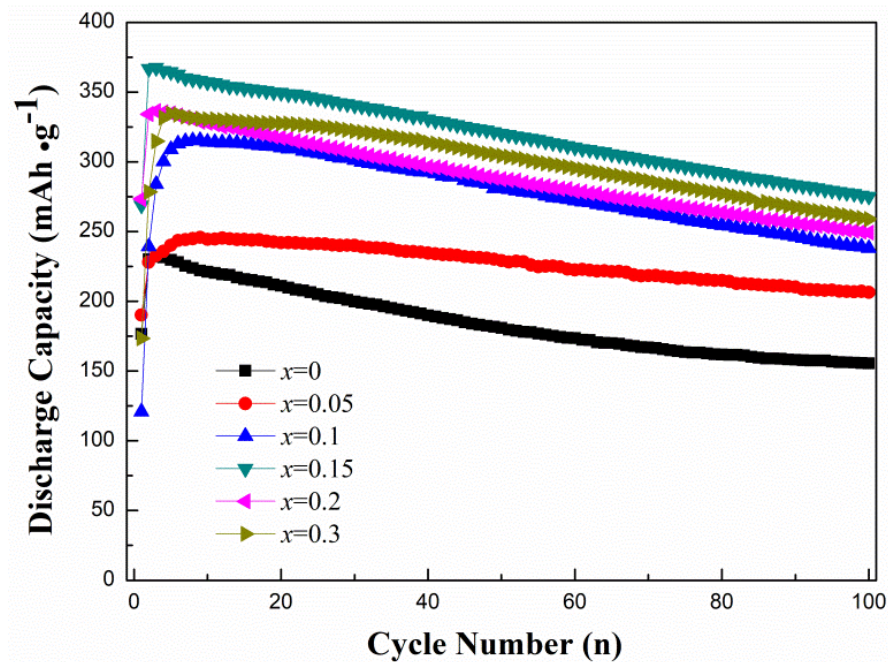


Figure 10. Cyclic stability curves of  $Y_{0.75}La_{0.25}Ni_{3.5-x}Mn_x$  ( $x = 0-0.3$ ) alloy electrodes.

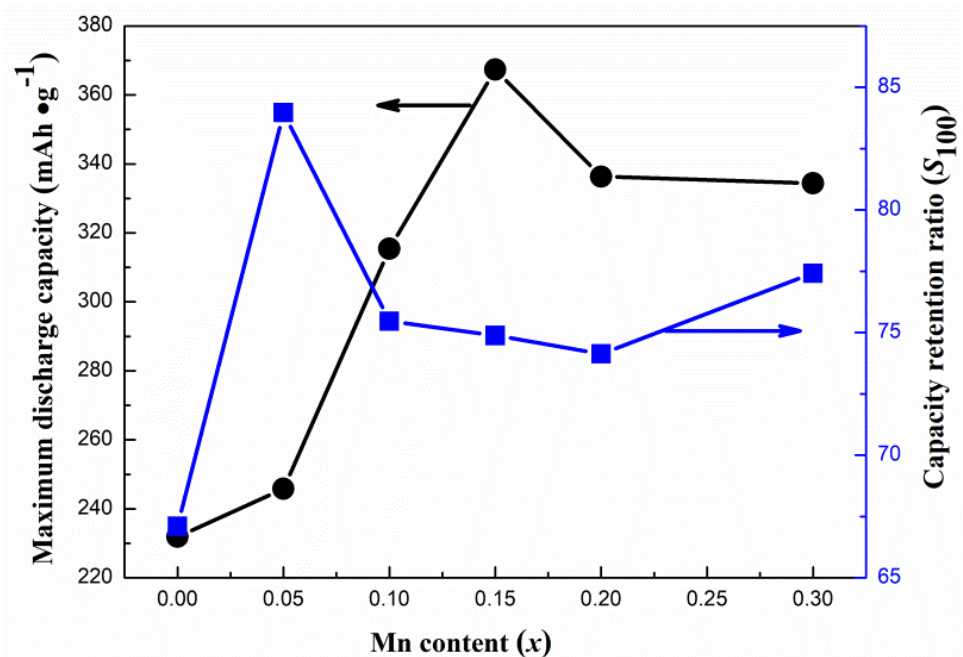


Figure 11. Maximum discharge capacity and capacity retention ratio after 100 cycles of  $Y_{0.75}La_{0.25}Ni_{3.5-x}Mn_x$  ( $x = 0-0.3$ ) alloy electrodes at 298 K.

From the gaseous  $P$ - $C$ - $T$  curves of the alloys previously discussed, it can be seen that with the increase in  $x$ , the maximum discharge capacity of the alloy electrodes first increases and then decreases. When  $x = 0-0.15$ , the gradual increase in discharge capacity is due to the increasing unit cell volume of each phase after the addition of Mn, which effectively reduces the hydrogen absorption and desorption plateau pressure of the alloy electrodes; when  $x = 0.15-0.3$ , the gradual decrease in discharge capacity may be mainly due to the fact that the hydrogen absorption/desorption plateau pressure of the alloy was too low, which made it difficult to release hydrogen. The hydrogen absorption/desorption plateau pressure between 0.01 and 0.1 MPa is most suitable for the alloy electrodes to absorb and desorb hydrogen. When the plateau pressure is too high, the hydrogen atoms will not be

absorbed by the alloys, and hydrogen will be released; on the other hand, when the plateau pressure is too low, the form of hydrogen in the hydride will change, and the discharge voltage and battery capacity will be reduced.

**Table 4.** Electrochemical properties of  $Y_{0.75}La_{0.25}Ni_{3.5-x}Mn_x$  ( $x = 0-0.3$ ) alloy electrodes.

Sample ( $x$ )	$N_a$	$C_{max}$	$S_{100}$	$i_{corr}$	$E_{corr}$
		( $mAh \cdot g^{-1}$ )	(%)	( $mA \cdot cm^{-2}$ )	(V)
$x = 0$	3	231.9	67.1	10.1	-0.934
$x = 0.05$	9	245.8	84.0		
$x = 0.1$	9	315.4	75.5	9.53	-0.93
$x = 0.15$	3	367.4	74.9		
$x = 0.2$	3	336.3	74.1		
$x = 0.3$	5	334.4	77.4	3.85	-0.925

The capacity degradation of alloy electrodes is mainly ascribed to structural failure (hydrogen-induced amorphization, hydrogen-induced phase transformation, hydrogen-induced defects, stress-strain, etc.) and the electrochemical corrosion of active materials during cycling. Since Mn is mainly distributed in the  $[AB_5]$  subunit, with the increase in Mn content, the mismatch between the  $[A_2B_4]$  and  $[AB_5]$  subunits is reduced; meanwhile, the structural stability of the alloy electrodes during electrochemical cycling is enhanced. At the same time, in general, the micro-strain resulting from the lattice expansion/contraction can lead to the pulverization of the alloy particles during the hydrogenation/dehydrogenation cycles; as a result, more and more fresh surfaces of alloy particles are directly exposed to alkaline electrolytes, which will accelerate the corrosion of the alloy electrodes [42]. According to this study, with the increase in Mn, the mismatch between the  $[A_2B_4]$  and  $[AB_5]$  subunits, micro-strain, and pulverization of alloys will all decrease, which reduces the corrosion of the alloys and improves the cycle stability of the alloy electrodes. Figure 12 shows the Tafel polarization curves of the alloy electrodes. It can be seen that with the increase in Mn content, the corrosion current density ( $i_{corr}$ ) decreased from  $10.1 mA \cdot cm^{-2}$  ( $x = 0$ ) to  $3.85 mA \cdot cm^{-2}$  ( $x = 0.3$ ) and the corrosion potential ( $E_{corr}$ ) decreased from  $-0.934 V$  ( $x = 0$ ) to  $-0.925 V$  ( $x = 0.3$ ), respectively. These results show that the addition of the Mn element reduces the corrosion behavior of alloy electrodes; this is consistent with the previous discussion. Hence, Mn-containing alloys will promote the cyclic stability of the alloy electrodes. From  $x = 0.1$  to  $x = 0.3$ , the cyclic stability  $S_{100}$  of the alloy electrodes did not change significantly, all between 74.88% and 77.42%, which indicates that the crystalline structure of the alloy has been maintained well in the electrochemical charge/discharge process since  $x = 0.1$ .

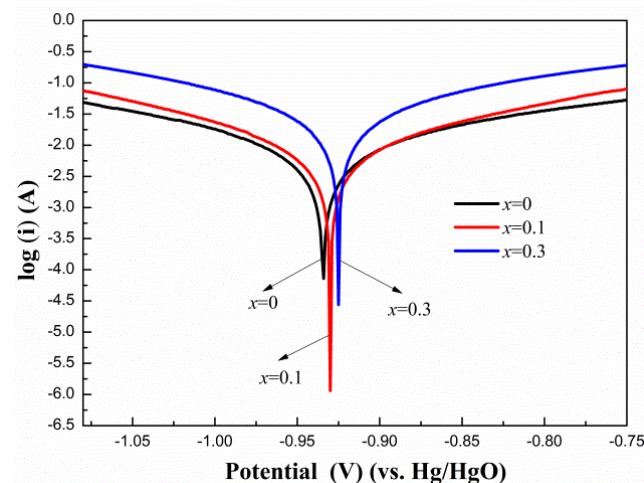


**Figure 12.** Tafel polarization curves of  $Y_{0.75}La_{0.25}Ni_{3.5-x}Mn_x$  ( $x = 0, 0.1, 0.3$ ) alloy electrodes.

#### 4. Conclusions

In this paper, the structures and properties of  $Y_{0.75}La_{0.25}Ni_{3.5-x}Mn_x$  ( $x = 0-0.3$ ) alloys were systematically investigated. Some conclusions can be summarized as follows:

- (1)  $Y_{0.75}La_{0.25}Ni_{3.5}$  alloy consisted of complex phases: PuNi<sub>3</sub>-type, Ce<sub>2</sub>Ni<sub>7</sub>-type, Gd<sub>2</sub>Co<sub>7</sub>-type, Ce<sub>5</sub>Co<sub>19</sub>-type and CaCu<sub>5</sub>-type phase. A small amount of Mn substitution for Ni does not change the phase structure of the alloys. With the increase in Mn content, the Gd<sub>2</sub>Co<sub>7</sub>-type phase turns into the Ce<sub>2</sub>Ni<sub>7</sub>-type phase. When the value of Mn is between 0.1 and 0.15, the single-phase property of the alloys is better, and the phase abundance of Ce<sub>2</sub>Ni<sub>7</sub>-type reaches more than 80%. Mn mainly occupies Ni sites in the [AB<sub>5</sub>] subunit and the interface between the [AB<sub>5</sub>] and [A<sub>2</sub>B<sub>4</sub>] subunits.
- (2) The maximum hydrogen absorption capacity of series alloys is 1.260 wt.%–1.444 wt.% under 8 MPa. When the Mn content increases, the maximum hydrogen absorption of the alloy increases first and then decreases. It increases from 1.339 wt.% ( $x = 0$ ) to 1.444 wt.% ( $x = 0.15$ ) and then decreases to 1.404 wt.% ( $x = 0.3$ ). The hydrogen desorption plateau pressure of the alloys gradually decreases, and the hydrogen absorption/desorption plateau pressure of the alloy becomes flatter and wider. The addition of Mn effectively improves the hydrogen absorption/desorption performance of the series alloys.
- (3) With the increase in Mn content, the maximum discharge capacity of the alloy electrodes first increased and then decreased, from 231.9 mAh·g<sup>-1</sup> ( $x = 0$ ) to 367.4 mAh·g<sup>-1</sup> ( $x = 0$ ), and then decreased to 334.4 mAh·g<sup>-1</sup> ( $x = 0$ ). The maximum discharge capacity of the alloy electrodes is closely related to its hydrogen storage capacity at 0.1 MPa and its hydrogen absorption/desorption plateau pressure. The cyclic stability of all the Mn-containing alloy electrodes was improved distinctly compared to that of Mn-free alloy electrodes, because the volume mismatch between the [A<sub>2</sub>B<sub>4</sub>] and [AB<sub>5</sub>] subunits of each phase for series alloys became smaller after the addition of Mn, which improved the structural stability and reduced the corrosion of the alloys during the hydrogen absorption/desorption cycles.

In summary, for  $Y_{0.75}La_{0.25}Ni_{3.5-x}Mn_x$  ( $x = 0-0.3$ ) alloys, there is an optimum Mn substitution ( $x = 0.1-0.15$ ) for Ni in terms of the structures, hydrogen storage behaviors, as well as the electrochemical properties of the alloys, in which the Ce<sub>2</sub>Ni<sub>7</sub>-type phase abundance is higher and the overall performance is better.

**Author Contributions:** A.D. and Y.L. conceived and designed the experiments; A.D. performed the experiments; A.D., J.Z., Y.X., Y.Y., X.K., B.S. and H.Z. analyzed the data; A.D. wrote the draft and Y.L. revised it. All authors have read and agreed to the published version of the manuscript.

**Funding:** This work was funded by the National Natural Science Foundation of China (No. 51761026), Ningxia Natural Science Fund (No. 2022AAC03048 and 2019AAC03003) and the fund of the State Key Laboratory of Advanced Processing and Recycling of Non-Ferrous Metals (No. SKLAB02019004), Lanzhou University of Technology.

**Conflicts of Interest:** The authors declare no conflict of interest.

#### References

1. Orzech, M.W.; Mazzali, F.; McGettrick, J.D.; Pleydell-Pearce, C.; Watson, T.M.; Voice, W.; Jarvis, D.; Margadonna, S. Synergic effect of Bi, Sb and Te for the increased stability of bulk alloying anodes for sodium-ion batteries. *J. Mater. Chem.* **2017**, *44*, 23198–23208. [[CrossRef](#)]
2. Young, K.H.; Nei, J. The Current Status of Hydrogen Storage Alloy Development for Electrochemical Applications. *Materials* **2013**, *10*, 4574–4608. [[CrossRef](#)] [[PubMed](#)]
3. Ouyang, L.; Huang, J.; Wang, H.; Liu, J.; Zhu, M. Progress of hydrogen storage alloys for Ni-MH rechargeable power batteries in electric vehicles: A review. *Mater. Chem. Phys.* **2017**, *200*, 164–178. [[CrossRef](#)]
4. Khazaeli, A.; Barz, D.P.J. Fabrication and characterization of a coplanar nickel-metal hydride microbattery equipped with a gel electrolyte. *J. Power Sources* **2019**, *414*, 141–149. [[CrossRef](#)]

5. Wang, W.; Qin, R.; Wu, R.; Tao, X.; Zhang, H.; Ding, Z.; Fu, Y.; Zhang, L.; Wu, L.; Li, Y.; et al. A promising anode candidate for rechargeable nickel metal hydride power battery: An  $A_5B_{19}$ -type La–Sm–Nd–Mg–Ni–Al-based hydrogen storage alloy. *J. Power Sources* **2020**, *465*, 228236. [[CrossRef](#)]
6. Zhang, L.; Jia, Z.; Wang, W.; Rodríguez-Pérez, I.A.; Zhao, Y.; Li, Y.; Zhao, X.; Wang, L.; Han, S. A new choice for the anode of nickel metal hydride batteries with long cycling life: A  $Ce_2Ni_7$ -type single-phase  $Nd_{0.80}Mg_{0.20}Ni_{3.58}$  hydrogen storage alloy. *J. Power Sources* **2019**, *433*, 126687. [[CrossRef](#)]
7. Tarasov, B.P.; Fursikov, P.V.; Volodin, A.A.; Bocharnikov, M.S.; Shimkus, Y.Y.; Kashin, A.M.; Yartys, V.A.; Chidziva, S.; Pasupathi, S.; Lototsky, M.V. Metal hydride hydrogen storage and compression systems for energy storage technologies. *Int. J. Hydrog. Energy* **2020**, *46*, 13647–13657. [[CrossRef](#)]
8. Young, K.; Ouchi, T.; Wang, L.; Wong, D.F. The effects of Al substitution on the phase abundance, structure and electrochemical performance of  $La_{0.7}Mg_{0.3}Ni_{2.8}Co_{0.5-x}Al_x$  ( $x = 0, 0.1, 0.2$ ) alloys. *J. Power Sources* **2015**, *279*, 172–179. [[CrossRef](#)]
9. Qiu, S.; Huang, J.; Chu, H.; Zou, Y.; Xiang, C.; Zhang, H.; Xu, F.; Sun, L.; Ouyang, L.; Zhou, H. Influence of Zr Addition on Structure and Performance of Rare Earth Mg-Based Alloys as Anodes in Ni/MH Battery. *Metals* **2015**, *5*, 565–577. [[CrossRef](#)]
10. Zhang, Q.; Zhao, B.; Fang, M.; Liu, C.; Hu, Q.; Fang, F.; Sun, D.; Ouyang, L.; Zhu, M.  $(Nd_{1.5}Mg_{0.5})Ni_7$ -based compounds: Structural and hydrogen storage properties. *Inorg. Chem.* **2012**, *51*, 2976–2983. [[CrossRef](#)]
11. Pan, H.; Jin, Q.; Gao, M.; Liu, Y.; Li, R.; Lei, Y.; Wang, Q. An electrochemical study of  $La_{0.4}Ce_{0.3}Mg_{0.3}Ni_{2.975-x}Mn_xCo_{0.525}$  ( $x = 0.1-0.4$ ) hydrogen storage alloys. *J. Alloys Compd.* **2004**, *376*, 196–204. [[CrossRef](#)]
12. Kadir, K.; Sakai, T.; Uehara, I. Synthesis and structure determination of a new series of hydrogen storage alloys;  $RMg_2Ni_9$  ( $R = La, Ce, Pr, Nd, Sm$  and  $Gd$ ) built from  $MgNi_2$  Laves-type layers alternating with  $AB_5$  layers. *J. Alloys Compd.* **1997**, *257*, 115–121. [[CrossRef](#)]
13. Kohno, T.; Yoshida, H.; Kawashima, F.; Inaba, T.; Sakai, I.; Yamamoto, M.; Kanda, M. Hydrogen storage properties of new ternary system alloys:  $La_2MgNi_9$ ,  $La_5Mg_2Ni_{23}$ ,  $La_3MgNi_{14}$ . *J. Alloys Compd.* **2000**, *311*, L5–L7. [[CrossRef](#)]
14. Liu, Y.; Yuan, H.; Guo, M.; Jiang, L. Effect of Y element on cyclic stability of  $A_2B_7$ -type La–Y–Ni-based hydrogen storage alloy. *Int. J. Hydrog. Energy* **2019**, *44*, 22064–22073. [[CrossRef](#)]
15. Zhao, S.; Wang, H.; Yang, L.; Liu, J.; Ouyang, L.; Zhu, M. Modulating superlattice structure and cyclic stability of  $Ce_2Ni_7$ -type  $LaY_2Ni_{10.5}$ -based alloys by Mn, Al, and Zr substitutions. *J. Power Sources* **2022**, *524*, 231067. [[CrossRef](#)]
16. Crivello, J.C.; Paul-Boncour, V. Relation between the weak itinerant magnetism in  $A_2Ni_7$  compounds ( $A = Y, La$ ) and their stacked crystal structures. *J. Phys. Condens. Matter.* **2020**, *32*, 145802. [[CrossRef](#)]
17. Iwase, K.; Sakaki, K.; Nakamura, Y.; Akiba, E. In situ XRD study of  $La_2Ni_7H_x$  during hydrogen absorption-desorption. *Inorg. Chem.* **2013**, *52*, 10105–10111. [[CrossRef](#)]
18. Chung, U.I.; Lee, J.-Y. A study on hydrogen-induced amorphization in the La–Ni system. *J. Non-Cryst. Solids* **1989**, *110*, 203–210. [[CrossRef](#)]
19. Oesterreicher, H.; Clinton, J.; Bittner, H. Hydrides of La–Ni compounds. *Mater. Res. Bull.* **1976**, *11*, 1241–1247. [[CrossRef](#)]
20. Denys, R.V.; Riabov, A.B.; Yartys, V.A.; Sato, M.; Delaplane, R.G. Mg substitution effect on the hydrogenation behaviour, thermodynamic and structural properties of the  $La_2Ni_7-H(D)_2$  system. *J. Solid State Chem.* **2008**, *181*, 812–821. [[CrossRef](#)]
21. Gal, L.; Charbonnier, V.; Zhang, J.; Goubault, L.; Bernard, P.; Latroche, M. Optimization of the La substitution by Mg in the  $La_2Ni_7$  hydride-forming system for use as negative electrode in Ni–MH battery. *Int. J. Hydrog. Energy* **2015**, *40*, 17017–17020. [[CrossRef](#)]
22. Charbonnier, V.; Zhang, J.; Monnier, J.; Goubault, L.; Bernard, P.; Magén, C.; Serin, V.; Latroche, M. Structural and Hydrogen Storage Properties of  $Y_2Ni_7$  Deuterides Studied by Neutron Powder Diffraction. *J. Phys. Chem. C* **2015**, *119*, 12218–12225. [[CrossRef](#)]
23. Paul-Boncour, V.; Crivello, J.C.; Madern, N.; Zhang, J.; Diop, L.V.B.; Charbonnier, V.; Monnier, J.; Latroche, M. Correlations between stacked structures and weak itinerant magnetic properties of  $La_{2-x}Y_xNi_7$  compounds. *J. Phys. Condens. Matter.* **2020**, *32*, 415804. [[CrossRef](#)] [[PubMed](#)]
24. Lartigue, C.; Percheron-Guégan, A.; Achard, J.C.; Tasset, F. Thermodynamic and structural properties of  $LaNi_{5-x}Mn_x$  compounds and their related hydrides. *J. Less Common Met.* **1980**, *75*, 23–29. [[CrossRef](#)]
25. Zhang, X.B.; Sun, D.Z.; Yin, W.Y.; Chai, Y.J.; Zhao, M.S. Effect of Mn content on the structure and electrochemical characteristics of  $La_{0.7}Mg_{0.3}Ni_{2.975-x}Co_{0.525}Mn_x$  ( $x = 0-0.4$ ) hydrogen storage alloys. *Electrochim. Acta* **2005**, *50*, 2911–2918. [[CrossRef](#)]
26. Liao, B.; Lei, Y.Q.; Chen, L.X.; Lu, G.L.; Pan, H.G.; Wang, Q.D. A study on the structure and electrochemical properties of  $La_2Mg(Ni_{0.95}M_{0.05})_9$  ( $M = Co, Mn, Fe, Al, Cu, Sn$ ) hydrogen storage electrode alloys. *J. Alloys Compd.* **2004**, *376*, 186–195. [[CrossRef](#)]
27. Liu, Y.; Pan, H.; Zhu, Y.; Li, R.; Lei, Y. Influence of Mn content on the structural and electrochemical properties of the  $La_{0.7}Mg_{0.3}Ni_{4.25-x}Co_{0.75}Mn_x$  hydrogen storage alloys. *Mater. Sci. Eng. A* **2004**, *372*, 163–172. [[CrossRef](#)]
28. Zhang, F.; Luo, Y.; Chen, J.; Yan, R.; Kang, L.; Chen, J. Effect of annealing treatment on structure and electrochemical properties of  $La_{0.67}Mg_{0.33}Ni_{2.5}Co_{0.5}$  alloy electrodes. *J. Power Sources* **2005**, *150*, 247–254. [[CrossRef](#)]
29. Li, Y.; Liu, Z.; Zhang, G.; Zhang, Y.; Ren, H. Single phase  $A_2B_7$ -type La–Mg–Ni alloy with improved electrochemical properties prepared by melt-spinning and annealing. *J. Rare Earths* **2019**, *37*, 1305–1311. [[CrossRef](#)]
30. Wang, W.; Xu, G.; Zhang, L.; Ma, C.; Zhao, Y.; Zhang, H.; Ding, Z.; Fu, Y.; Li, Y.; Han, S. Electrochemical features of  $Ce_2Ni_7$ -type  $La_{0.65}Nd_{0.15}Mg_{0.25}Ni_{3.20}M_{0.10}$  ( $M = Ni, Mn$  and  $Al$ ) hydrogen storage alloys for rechargeable nickel metal hydride battery. *J. Alloys Compd.* **2021**, *861*, 158469. [[CrossRef](#)]

31. Young, R.A. *The Rietveld Method*; Oxford University Press: New York, NY, USA, 1993; pp. 1–38.
32. Rodríguez-Carvajal, J. Recent advances in magnetic structure determination by neutron powder diffraction. *Phys. B* **1993**, *192*, 55. [[CrossRef](#)]
33. Si, T.; Zhang, Q.; Liu, N. Phase structure and electrochemical properties of laser sintered La<sub>2</sub>MgNi<sub>9</sub> hydrogen storage electrode alloys. *J. Rare Earths* **2008**, *26*, 598–603. [[CrossRef](#)]
34. Buschow, K.H.J.; Van Der Goot, A.S. The crystal structure of rare-earth nickel compounds of the type R<sub>2</sub>Ni<sub>7</sub>. *J. Less Common Met.* **1970**, *22*, 419–428. [[CrossRef](#)]
35. Sears, V.F. Neutron scattering lengths and cross sections. *Neutron News* **2006**, *3*, 26–37. [[CrossRef](#)]
36. Khan, Y. The crystal structure of R<sub>5</sub>Co<sub>19</sub>. *Acta Crystallogr. Sect. B Struct. Crystallogr. Crystal Chem.* **1974**, *30*, 1533–1537. [[CrossRef](#)]
37. Denys, R.V.; Riabov, B.; Yartys, V.A.; Delaplane, R.G.; Sato, M. Hydrogen storage properties and structure of La<sub>1-x</sub>Mg<sub>x</sub>(Ni<sub>1-y</sub>Mn<sub>y</sub>)<sub>3</sub> intermetallics and their hydrides. *J. Alloys Compd.* **2007**, *446–447*, 166–172. [[CrossRef](#)]
38. Fang, F.; Chen, Z.; Wu, D.; Liu, H.; Dong, C.; Song, Y.; Sun, D. Subunit volume control mechanism for dehydrogenation performance of AB<sub>3</sub>-type superlattice intermetallics. *J. Power Sources* **2019**, *427*, 145–153. [[CrossRef](#)]
39. Zhang, J.; Charbonnier, V.; Madern, N.; Monnier, J.; Latroche, M. Improvement of reversible H storage capacity by fine tuning of the composition in the pseudo-binary systems A<sub>2-x</sub>La<sub>x</sub>Ni<sub>7</sub> (A = Gd, Sm, Y, Mg). *J. Alloys Compd.* **2021**, *852*, 157008. [[CrossRef](#)]
40. Liu, J.; Li, Y.; Han, D.; Yang, S.; Chen, X.; Zhang, L.; Han, S. Electrochemical performance and capacity degradation mechanism of single-phase La–Mg–Ni-based hydrogen storage alloys. *J. Power Sources* **2015**, *300*, 77–86. [[CrossRef](#)]
41. Xiong, W.; Yan, H.; Wang, L.; Verbetsky, V.; Zhao, X.; Mitrokhin, S.; Li, B.; Li, J.; Wang, Y. Characteristics of A<sub>2</sub>B<sub>7</sub>-type La–Y–Ni-based hydrogen storage alloys modified by partially substituting Ni with Mn. *Int. J. Hydrog. Energy* **2017**, *42*, 10131–10141. [[CrossRef](#)]
42. Liu, Y.; Pan, H.; Yue, Y.; Wu, X.; Chen, N.; Lei, Y. Cycling durability and degradation behavior of La–Mg–Ni–Co-type metal hydride electrodes. *J. Alloys Compd.* **2005**, *395*, 291–299. [[CrossRef](#)]